Copper-Substituted Calcium Orthophosphate (CaxCu1-x)HPO4.nH2O for Humidity Detection

Original
Copper-Substituted Calcium Orthophosphate (CaxCu1-x)HPO4.nH2O for Humidity Detection / Milovanov, Yurii; Dadkhah, Mehran; Sabry Afify, Ahmed; Tulliani, Jean-Marc. - In: CRYSTALS. - ISSN 2073-4352. - ELETTRONICO. - 15:2(2025). [10.3390/cryst15020153]

Publisher:
MDPI

Published
DOI:10.3390/cryst15020153

crystals

MDPI

Article

Copper-Substituted Calcium Orthophosphate $(Ca_xCu_{1-x})HPO_4.nH_2O$ for Humidity Detection

Yurii Milovanov [1], Mehran Dadkhah [1], Ahmed Sabry Afify [2] and Jean-Marc Tulliani [1,*]

[1] Department of Applied Science and Technology, Politecnico di Torino, INSTM R.U. Lince Laboratory, Corso Duca degli Abruzzi 24, 10129 Turin, Italy; yurii.milovanov@polito.it (Y.M.); mehran.dadkhah@polito.it (M.D.)
[2] Department of Basic Sciences, The Higher Institute of Engineering and Automotive Technology and Energy, New Heliopolis 11829, Egypt; ahmedsabryafify@yahoo.com
* Correspondence: jeanmarc.tulliani@polito.it; Tel.: +39-0110904700

Abstract: Calcium orthophosphate material $(Ca_{1-x}Cu_x)HPO_4.nH_2O$ ($0.4 \leq x \leq 1$) with the gradual replacement of Ca^{2+} with Cu^{2+} ions were synthesized by a chemical precipitation technique. Samples were characterized by X-ray diffraction (XRD), scanning electron microscopy (SEM) and transmission electron microscopy (TEM). Then, the prepared powders were deposited onto an alumina substrate with interdigitated Pt electrodes by the spin coating method and polyvinyl alcohol (PVA) as a binder. Successively, the sensors were investigated from 0% to 90% at room temperature under various conditions, including humidity, nitrogenous oxide, methane, carbon dioxide and ammonia. The results evidenced that at 90% RH, the sensitivity of sensors significantly increased with the increase in the Cu content. Moreover, the sensors exhibited good repeatability and, after 1 year of aging, the sensor response was equal to 34% that of the freshly prepared sensor. Finally, there was no interference in the presence of other gases (nitrogenous oxide 2.5 ppm, methane 10 ppm, carbon dioxide 500 ppm and ammonia 4 ppm).

Keywords: brushite; DCPD; sampleite; humidity sensor; relative humidity; spin coating

check for updates

Academic Editor: Zongyou Yin

Received: 30 December 2024
Revised: 27 January 2025
Accepted: 28 January 2025
Published: 1 February 2025

Citation: Milovanov, Y.; Dadkhah, M.; Afify, A.S.; Tulliani, J.-M. Copper-Substituted Calcium Orthophosphate $(Ca_xCu_{1-x})HPO_4.nH_2O$ for Humidity Detection. *Crystals* **2025**, *15*, 153. https://doi.org/10.3390/cryst15020153

1. Introduction

Relative humidity (RH) monitoring and control are of primary importance for different sectors of industry, such as healthcare (in hospital operating rooms, respiratory equipment, incubators, etc.), food processing, textile technology, laundry, leather, paper, semiconductor and petrochemical industries, environmental monitoring, agriculture (crop protection and soil relative humidity monitoring), and automation (air conditioning, etc.) [1–7]. Cheap humidity sensors with high sensitivity, selectivity, and fast response times are fundamental for humidity detection. Thus, there is still a need for new sensors with higher sensitivity and repeatability. Throughout the years and to satisfy the increasing demand, many different humidity sensors have been developed. These sensors can be classified in function of the signal types, which include optical, acoustic frequency, voltage-based humidity, capacitive-based and impedance sensors [6–10].

Among optical systems, fiber optic sensors are the most popular [8]. They consist of at least three components: a core, cladding, and a light-impermeable (protective) jacket. The core is the fiber made either of glass, acrylic or perfluorinated polymers, silica, or other ceramics where the light travels. The cladding surrounds the fiber and reflects the light back into the core according to the total internal reflection principle [8]. In the case of lossy mode resonance (LMR) sensors, part of the cladding is removed, and a thin film of indium tin oxide (ITO) is applied, allowing for the adsorption of water molecules. When this happens, the effective refractive index of ITO increases, and the LMR wavelength shifts to greater values [8]. Other devices are optical hygrometers. They have a mirror whose surface temperature is accurately controlled at a threshold of the formation of dew. When air passes over the mirror surface, moisture is released in the form of water droplets. Then, the reflective properties of the mirror change because water droplets scatter light rays and are detected by a photodetector [9].

Mass-sensitive gas sensors like microcantilever, quartz crystal microbalance (QCM), and surface acoustic wave (SAW)-based sensors rely on the sensors' mass changes when water molecules adsorb [10]. These mass variations can be detected either by the deflection of a micromechanical structure or by measuring the frequency shift of a resonating structure or of a traveling acoustic wave.

The thermal conductivity of a gas can be used for measuring humidity by means of a differential thermistor-based sensor with two tiny thermistors. One of them is exposed to the outside gas, while the second one is kept in dry air in a hermetically sealed cell. Both thermistors are connected into a bridge circuit powered by a reference voltage and produce heat due to the passage of a current by the Joule effect [9].

Capacitive humidity sensors make use of a polymeric layer, which acts as sensitive material and adsorbs water molecules from the atmosphere. Because water has a high dielectric constant, when the number of adsorbed molecules increases, the capacitance of the sensor rises as well. Capacitive sensors are based either on ceramics, like alumina, or on polymers and have the advantage of being sensitive over a wide range of humidity values [8]. However, resistive/impedance humidity sensors are simpler and easier to produce with respect to capacitive ones, and they do not suffer from the existence of parasitic capacitance. Resistive-type humidity sensors are based on the electrical resistivity changes in conductive polymers, semiconductors or composites because of water molecule adsorption [8]. Resistive humidity sensors were selected for this work because of their simple manufacturing process and low cost. In recent years, different ceramic materials were studied, including SnO_2 [11], ZnO [11], In_2O_3 [11], Fe_2O_3 [11], Fe_3O_4 [11], TiO_2 [11,12], WO_3 [11,13], modified sepiolite [14], glass ceramics [15], perovskites [11,16–19], and other oxides [11].

Calcium orthophosphates constitute an important family of compounds with different Ca/P ratios and structural water contents. Among them, we can find the mineral dicalcium phosphate dihydrate (DCPD, $CaHPO_4.2H_2O$) also known as brushite. It can be used in different environmental, medical, agriculture and pharmacy applications, like implants [20] and fertilizers [21]. DCPD has high porosity, high adsorption capacity, and good biocompatibility, making it a promising candidate for sensor applications [22–25]. Sánchez-Paniagua López et al. [23] fabricated a highly sensitive amperometric biosensor based on a biocompatible DCPD cement. This sensor quickly detected phenolic compounds in both aqueous and non-aqueous media. Moreover, the biosensor was effective in analyzing real wastewater samples collected from an olive oil refinement facility, demonstrating its analytical suitability for complex samples. Sudhan et al. [24] prepared an electrochemical sensor based on DCPD nanoparticles for either the independent or simultaneous determination of uric acid, xanthine, hypoxanthine and caffeine. In another study, electrochemical tyrosinase biosensors for tyramine determination were developed by immobilizing an enzyme in calcium phosphate materials and cross-linking with glutaraldehyde.

However, to the best of our the knowledge of the authors, DCPD has never been used before as a humidity-sensing material; thus, in this research paper, the humidity-sensing properties of $(Ca_{1-x}Cu_x)HPO_4.nH_2O$ ($0.4 \leq x \leq 1$) thick films prepared by the spin-coating method were investigated. Their electrical responses with respect to humidity and to interfering gases (CO_2, NO_2, CH_4 and NH_3) were then studied for the first time.

2. Materials and Methods

2.1. Synthesis of $Ca_xM_{1\text{-}x}HPO_4.nH_2O$ Compounds

Sodium dihydrogen orthophosphate dihydrate ($Na_2HPO_4.2H_2O$) was purchased from Techno Pharmchem, New Delhi, India, while calcium nitrate tetrahydrate ($Ca(NO_3)_2.4H_2O$), copper(II) nitrate trihydrate and ammonium hydroxide solution, NH_4OH, were all provided by LOBA Chemie, Mumbai, India. Distilled water (0.055 µS/cm) was prepared using a water purification system (PURELAB Option-Q, ELGA, High Wycombe, Cheshire, UK). A digital analytical balance (EX324N, OHAUS, Parsippany, NJ, USA), a magnetic stirrer (ISOTEMP, Fisher Scientific, Shanghai, China), a pH meter (Adwa, Szeged, Hungary) and an electric oven (ED53/E2, Binder, Tuttlingen, Germany) were used when required.

The $(Ca_xCu_{1\text{-}x})HPO_4.nH_2O$ compounds are prepared at room temperature (RT) according to Equation (1) and are summarized in Table 1, where M is the molar proportions of the prepared solutions. The pH dropped down below 4.5 during the synthesis and an ammonia solution (25%) was added to achieve a pH = 6–6.5, as well as diluted HCl [26]. A low pH favors DCPD decomposition at room temperature into $CaHPO_4$ (monetite, dicalcium phosphate, DCP, another calcium orthophosphate) [27].

$$\begin{aligned} &\alpha Cu(NO_3)_2.3H_2O + (1-\alpha)Ca(NO_3)_2.4H_2O + Na_2HPO_4.2H_2O + \alpha NH_4OH \\ &\rightarrow (Ca_{1-\alpha}Cu_\alpha)HPO_4\cdot 2H_2O + 2NaNO_3 + \alpha NH_3 + 4H_2O \end{aligned} \tag{1}$$

Table 1. Molar proportions of reagents to synthesize $Ca_xCu_{1\text{-}x}HPO_4.nH_2O$ compounds.

Product ID	$NaH_2PO_4.2H_2O$	$Ca(NO_3)_2.4H_2O$	$Cu(NO_3)_2.3H_2O$	Cu/Ca Molar Ratio
BCu0	1	1	0	0
BCu4	1	0.6	0.4	0.67
BCu5	1	0.5	0.5	1.0
BCu10	1	0	1	-

Two precursors were prepared to obtain the brushite sample, denoted as BCu0, where the first one was 0.05 mol of $Ca(NO_3)_2.4H_2O$ and the second one was 0.05 mol of $Na_2HPO_4.2H_2O$, each one separately dissolved in 100 mL of deionized water. Subsequently, calcium solution was gradually added to phosphate solution at a 2 mL/min flow rate using a glass funnel with a glass stopcock under continuously stirring at 450 rpm for 2 h at RT until a 1.0 Ca/P molar ratio was achieved. The pH of the solution was adjusted to slightly acidic conditions of 6.0–6.5 using an ammonia solution (25% dilution) and diluted HCl. The white precipitate was then vacuum-filtered by means of a Buchner funnel and filter paper (45 µm, ∅12 cm, Double Rings, Shanghai, China). The obtained filter cake was washed using deionized water three times, followed by ethanol washing three times to overcome any agglomeration. The ratio of the synthesized powder in g to the volume of the deionized water in mL was 1:1.5, and the same ratio was used during rinsing with ethanol. Finally, the sample was dried at 40 °C overnight in an electric oven. The BCu4, BCu5, and BCu10 compounds were prepared by mixing $Ca(NO_3)_2.4H_2O$ and $Cu(NO_3)_2.3H_2O$ solutions according to the molar ratios in Table 1. Then, 100 mL of the resulting solution was added to $Na_2HPO_4.2H_2O$ solution at a 2 mL/min flow rate. From this step on, the preparation process was the same as for the sample BCu0 [26].

The powders were characterized by X-ray diffraction (XRD) by means of an Expert Pro Pan'Analytical diffractometer (Pan'Analytical, Worcestershire, UK) with CuKα radiation (λ = 0.154056 nm) in the 2θ range 5–70°. A time per step of 1 s and step size of 0.003° were used.

The microstructures of powders and of sensors were observed by means of field emission scanning electron microscopy (FESEM, Hitachi S4000, Tokyo, Japan) after sputtering the samples with platinum.

2.2. Preparation of the Ink and Sensing Film

Platinum electrodes were screen-printed (Ferro 5545, Kings of Prussia, USA; 2 successive prints) on alumina substrates using an automatic machine (Officine Baccini SPA model A2, Olmi di San Biagio di Callalta (TV), Italy) with a 270-mesh steel screen. After drying overnight, the Pt ink was heated at 980 °C for 15 min to increase the adhesion and optimize its electrical conductivity, according to the ink's producer recommendations. The electrodes were 400 μm thick and were spaced 450 μm one from each other.

The sensing ink was produced by dispersing 0.2 g of synthesized powder in 10 mL of ethanol through ultrasonic treatment (ArgoLab DU-32, Carpi (MO), Italy) for 2 h at 60 °C. Following this, 1% polyvinyl alcohol (PVA) solution was prepared by dissolving 1 g of PVA powder (PVA, Sigma Aldrich, Milan, Italy) in 99 mL of distilled water and stirred for 1 h at RT. Afterward, five drops of polyvinyl alcohol were gradually added to the solution. This was carried out to achieve the desired rheological characteristics, substrate adherence, and proper thermal shrinkage properties, ensuring, this way, the production of a high-quality film.

Moreover, the sensing film was prepared by depositing the obtained ink onto the interdigitated platinum electrodes using the spin coating method (SPS SPIN 150-V3 spin coater, Putten, The Netherlands). Spin coating was carried out at approximately 2000–2500 rpm for 1 min per layer. These films were dried at RT (approximately 25 °C) for 1 day. The formed sensing film had an area of about 1 cm^2 with good adhesion onto the substrates (Figure 1).

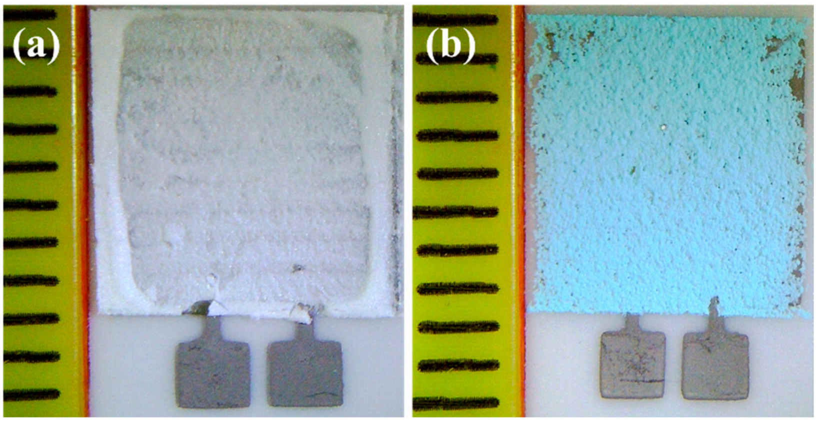

Figure 1. Optical micrograph of the sensor with screen-printed interdigitated electrodes: (**a**) BCu0 and (**b**) BCu10 (scale bar in mm).

The BCu4, BCu5 and BCu10 sensors were prepared with different deposited layers, specifically 2, 5, and 10 layers, denoted as 2L, 5L, and 10L, respectively, from now on.

2.3. Fabrication and Measurement of Gas Sensors

The sensor's humidity response in the 0–90% RH range was investigated in a laboratory apparatus at RT (23 °C), under an air flow rate of 150 mL/min. The RH was increased progressively by steps, each one lasting 15 min. In this system, the air flow (Siad, San Mauro Torinese (TO), Italy, research grade) was separated into two flows and controlled using mass flow controllers (MF302, Teledyne Hastings, Hampton, VA, USA; mass flow controller: Teledyne Power Pod 400): the first one was anhydrous, whereas the second one was sent to a water bubbler, producing a humid flow. Then, both flows were mixed. A commercial probe (Delta Ohm DO9406, Caselle di Selvazzano (PD), Italy; accuracy: ±0.1% in the 0–100% RH range and between 50 and 250 °C) was used for the determination of RH and temperature reference values [28]. During tests under a dynamic flow, the sensors' impedance modulus and phase were measured by an LCR meter (Hioki 3533-01, Ueda, Nagano, Japan). The alternating voltage was 1 V at a frequency of 1 kHz. This frequency was selected to limit any electric interference during the tests, with the network frequency value being enough different (50–60 Hz), while the applied tension was set to 1 V to prevent water electrolysis during the measurements in the presence of water vapor.

Additionally, cross-sensitivity tests were carried out for different gases like NH_3 (4 ppm in the air), CH_4 (10 ppm in the air), CO_2 (500 ppm in the air), and NO_2 (2.5 ppm in the air) under the same flow rate. Carbon dioxide is a common interfering gas in humidity detection, and the chosen concentration was close to the current one of the atmosphere (425.4 ppm [29]). Road traffic is the principal outdoor source of nitrogen dioxide, and annual mean concentrations of 10–50 ppb are reported [30]. CH_4 is a strong greenhouse gas that must be monitored, and its current concentration in air is about 1.9 ppm [31]. Ammonia is an irritating gas which can react with acidic species and form particulate matter. Its emissions are mostly due to agriculture, but in urban environments, the use of urea as a selective catalyst for reducing NOx emissions increases its concentration, which can reach up to 0.1 ppm [32]. The concentrations investigated in this work were the closest we could reach to the above-mentioned ones, considering the dilutions we could carry out with flowmeters and the concentration in the gas cylinders available in the laboratory.

The response of the sensor (R) was defined in accordance with Equation (2):

$$R = {}^{Z_0}/_{Z_g} \tag{2}$$

where Z_0 and Z_g are the impedance modulus of the sensor under dry and humid air, respectively.

The sensitivity (S) of the sensor is the slope of the calibration curve, and it can be determined by Equation (3):

$$S(Z) = {}^{\Delta Z}/_{\Delta RH} \tag{3}$$

The response time (the time required by a sensor to achieve 90% of the total impedance variation in the presence of humid air), as well as the recovery time (the time needed for a sensor to reach 90% of the total impedance change in the case of gas desorption), was calculated too.

3. Results and Discussion

3.1. Sensors' Microstructural Characterization

Optical micrographs of the printed sensors with screen-printed electrodes are reported in Figure 1: sample BCu0 is made of a white film (Figure 1a), while sample BCu10 appears blue after the complete substitution of calcium with copper (Figure 1b).

The XRD patterns of the studied materials are reported in Figure 2. Sample BC0 is a mixture of brushite and monetite. Samples BCu4 and BCu5 are made of a second phase with a structure close to sampleite and DCP. On the contrary, sample BCu10 is made mostly of a compound with a structure similar to sampleite. Neither tenorite (CuO, JCPDF card 48-1548) nor cuprite (Cu_2O, JCPDF card 05-0667) were detected, indicating that copper atoms entered into the structure of the different phases (DCP and sampleite). These results are in line with reports in the literature [26].

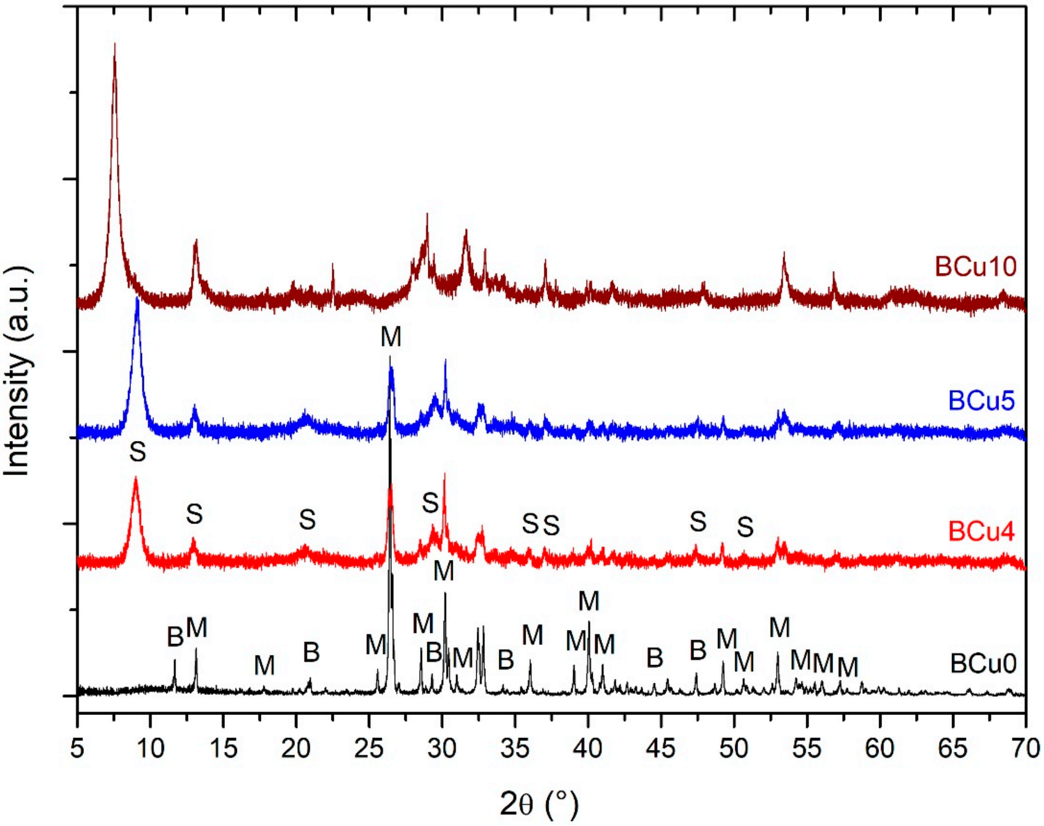

Figure 2. XRD patterns of the investigated sensing materials (B = DCPD, JCPDF card number 09-0077, M = DCP, JCPDF card number 09-0080, S = sampleite, JCPDF card number 11-0349).

Chlorine was probably incorporated into the structure of sampleite during the synthesis because of the use of a diluted HCl solution to adjust the pH in combination with ammonia. Sampleite and lavendulan ($NaCaCu_5(AsO_4)_4Cl.5H_2O$) possess similar structures, despite the different P—O and As—O distances (P—O = 0.155 nm and As—O = 0.1685 nm). Lavendulan is made of heteropolyhedral sheets of CuO_4Cl and AsO_4 groups bound via NaO_6 and CaO_7 polyhedra, as well as by hydrogen bonds into a loose framework. The CaO_7 polyhedron may be either an irregular or a distorted incomplete cube with two adjacent corners merged into one. They share two opposite edges with CuO_4Cl pyramids, and the other ligands are oxygen atoms from four water molecules. The replacement of Ca^{2+} by Cu^{2+} appears possible in the sampleite structure, though they have different ionic radii when in coordination 6 in octahedral sites (respectively, 114 pm and 87 pm) [33]. The increase in interlayer (Na and Ca) and Cl atoms per formula unit and a different interlayer connectivity could explain the shift in the main XRD peak to low 2θ angles due to an apparent increase in the unit cell volume.

The FESEM micrographs of the powders are presented in Figure 3. Characteristics of the morphology of DCPD include plate-like or needle-like structures, depending on the pH of the used solution [34], as observable in Figure 3a. In DCPD, the two water molecules link layers made of $CaHPO_4$ via hydrogen bonds, while DCP is anhydrous and does not have a layered structure [35]. Figure 3b,c show that BCu4 and BCu5 powders have similar crystal morphology and sizes of sampleite-like material comprising monoclinic crystals with a length of ≈5 μm. Finally, sample BCu10 appears to be made of smaller grains more agglomerated than the previous samples (Figure 3d).

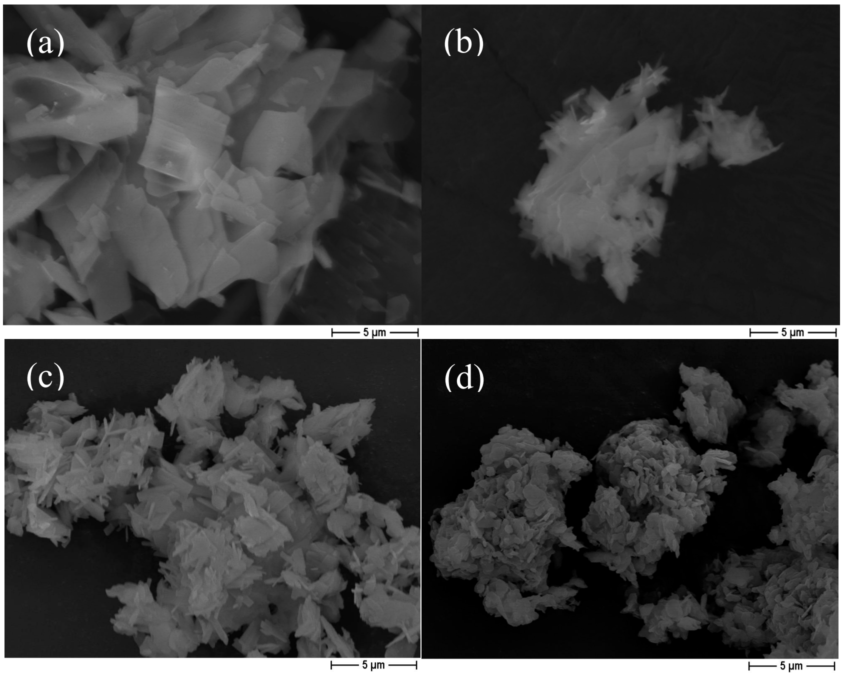

Figure 3. FESEM micrographs of the prepared powders: (**a**) BCu0, (**b**) BCu4, (**c**) BCu5 and (**d**) BCu10 (sputtering thickness for platinum coating is about 5 nm, magnification = 5000×).

The morphology and structure of the synthesized DCPD samples were also studied by TEM observations. Figure 4 shows the TEM micrograph of BCu0, showing that the particles have average dimensions of about 130 × 230 nm^2.

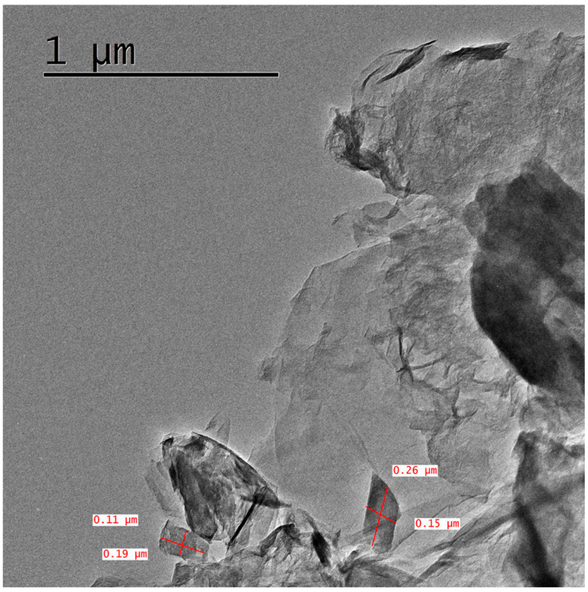

Figure 4. TEM micrograph of the BCu0 powder.

FESEM observations of the pristine PVA film (Figure 5a ×5000) showed an uncomplete coverage of the alumina grains from the substrate, which was a positive result in that it did not completely wrap the grains of the sensing material. The low-magnification micrograph (×500, Figure 5b) of the BCu10 film shows the presence of cracks, probably due to fast solvent evaporation during the deposition process. Higher magnification micrographs (Figure 5c ×5000 and Figure 5d ×25,000) reveal a porous microstructure, which was positivefavorable for humidity detection.

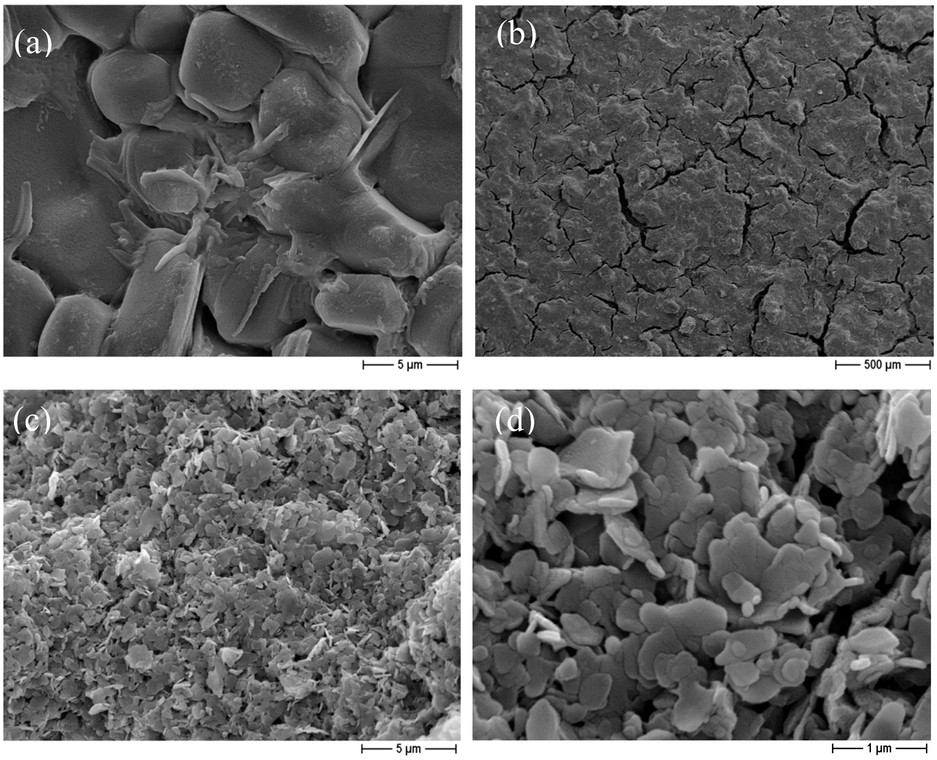

Figure 5. FESEM micrographs of the films: (**a**) pristine PVA (**b**), (**c**,**d**) BCu10 film.

FESEM observations on the side of BCu10 films allowed us to estimate their thickness, which was equal to approximately 2.9 ± 0.3 µm, 4.0 ± 0.4 µm and 5.7 ± 0.2 µm, respectively, for the BCu10_2L, BCu5_5L and BCu10_10L samples (average values of four measurements per film).

3.2. Humidity-Sensing Properties

As the first step, the BCu0_10L sensor response was investigated up to 90 RH%. It was found that sensor responses were negligible in comparison to BCu4_10L, BCu5_10L, and BCu10_10L (Figure S1, Supplementary Information).

The impedance variations in sensors BCu4_10L, BCu5_10L and BCu10_10L for the range of 28–90 RH% are plotted in Figure 6. Under dry air, the initial impedance modulus values were 104 MΩ for BCu10, 81 MΩ for BCu5_10L and 94 MΩ for BCu4_10L. It was found that the impedance value of all sensors decreased as the RH% increased. Under low RH values, the sensors had high resistance values as only a limited amount of water molecules were adsorbed. On the contrary, under high RH values, the sensors adsorbed more water molecules, causing their impedance to decrease. When exposed to water vapor, the sensor response values under 28 RH% increased by a factor of 43 for BCu10_10L, 1.4 for BCu5_10L and 1.3 for BCu4_10L (Figure 6a). However, under 50 RH%, it increased by a factor of 2264 for BCu10_10L, 31 for BCu5_10L and 6.3 for BCu4_10L (Figure 6b); under 90 RH%, it increased by a factor 43,750 for BCu10_10L, 5963 for BCu5_10L and 1907 for BCu4_10L (Figure 6c).

The sensitivity of the sensors dramatically increased with the increase in the content of Cu in the range 28–90% RH. Comparing the sensors' performance under 90% humidity, sensors BCu10_10L and BCu5_10L showed the highest sensitivity: 43,750 and 5963 RH^{-1}, respectively.

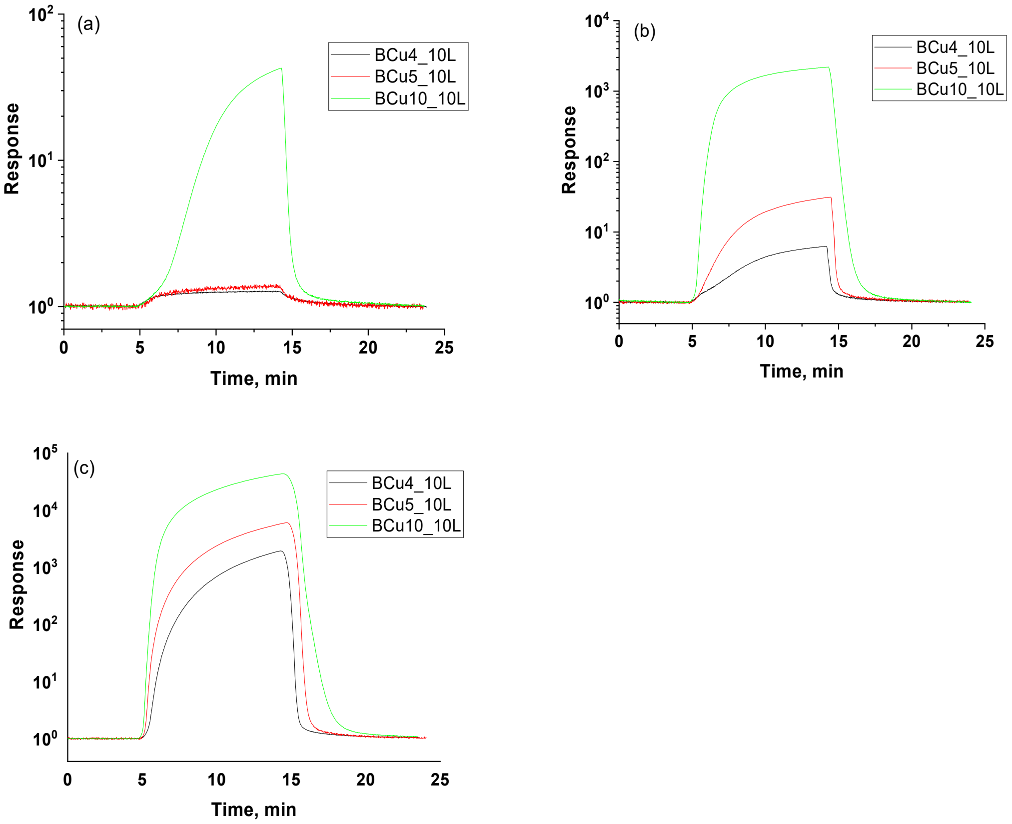

Figure 6. Sensor response in function of relative humidity value for BCu4_10L, BCu5_10L and BCu10_10L: (**a**) under 28% RH, (**b**) under 50% RH, (**c**) under 90% RH.

The next step was to investigate the dependence of the sensor response on the thickness of the sensing layer for sensors BCu5 and BCu10. The sensor response variations for BCu5_10L, BCu5_5L, and BCu5_2L are plotted in Figure 7. Under dry air, the initial impedance values were 106 MΩ for BCu5_2L, 101 MΩ for BCu5_5L and 81 MΩ for BCu5_10L.

When exposed to water vapor, the sensor response values under 28 RH% were 1.2 for BCu5_2L, 1.4 for BCu5_5L and 1.4 for BCu5_10L (Figure 7a). However, in the presence of 50 RH%, the sensor response values were 13 for BCu5_2L, 20 for BCu5_5L and 31 for BCu5_10L (Figure 7b), and under 90 RH%, it reached 4315 for BCu5_2L, 6265 for BCu5_5L and 5963 for BCu5_10L (Figure 7c).

The impedance variations in function of relative humidity in the range 12–90 RH% for BCu10_10L, BCu10_5L, and BCu10_2L are presented in Figure 8.

Under dry air condition, the initial impedance values were measured at 103 MΩ for BCu10_2L, 119 MΩ for BCu10_5L and 104 MΩ for BCu10_10L.

Nevertheless, the sensor response values showed significant variation when exposed to water vapor at varying RH%. As can be seen in Figure 8a, at 12% RH, the sensor response is 1.1 for both BCu10_5L and BCu10_10L. When the humidity increased to 20%, the response values enhanced to 1.6 for BCu10_2L, 2.5 for BCu10_5L and 3.6 for BCu10_10L (Figure 8b). Further increases were observed at 28% RH, where the responses reached 20 for BCu10_2L, 29 for BCu10_5L, and 43 for BCu10_10L (Figure 8c). At 50% RH, the response values increased dramatically to 907 for BCu10_2L, 1664 for BCu10_5L, and 2264 for BCu10_10L (Figure 8d). Furthermore, under 90% RH, the response values peaked at 26,892 for BCu10_2L, 51,250 for BCu10_5L, and 43,750 for BCu10_10L (Figure 8e).

When comparing the sensors' performance under 90% humidity for different deposition layer thicknesses, both BCu10 and BCu5 showed the highest sensor responses, reaching 51,250 with five layers of deposition for BCu10_5L and 6265 for BCu5_5L.

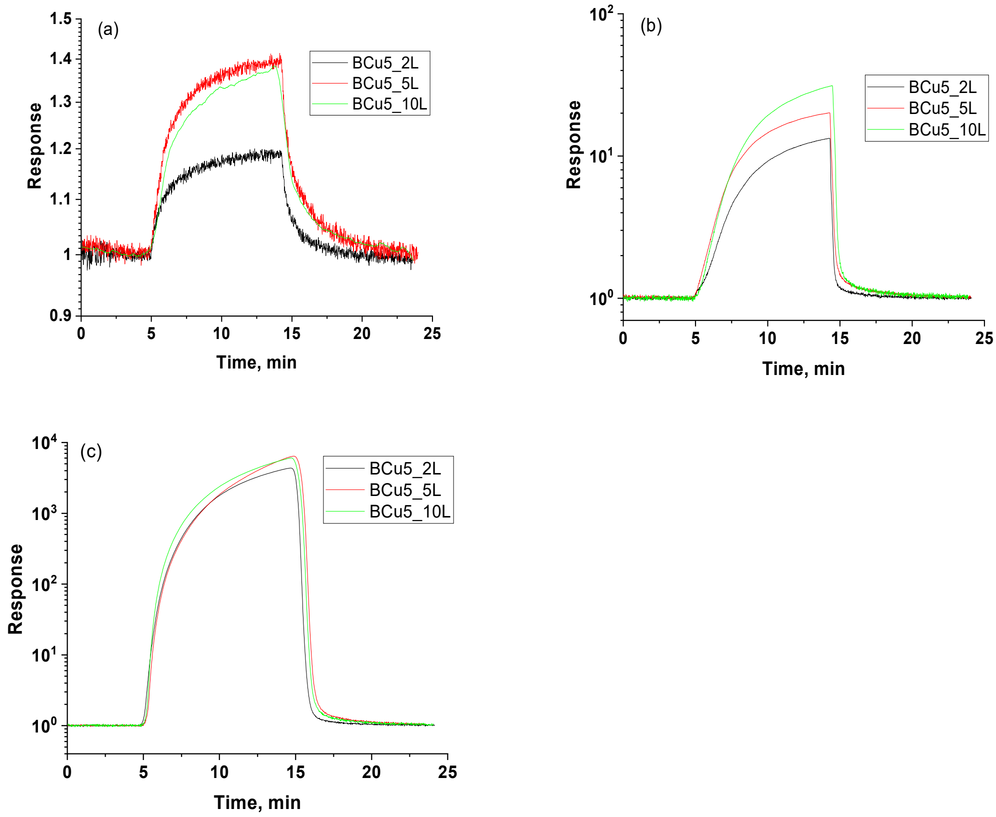

Figure 7. Sensor response in function of relative humidity value for BCu5_10L, BCu5_5L, and BCu5_2L: (**a**) under 28% RH, (**b**) under 50% RH, and (**c**) under 90% RH.

The sensors' responses, along with response times (the time taken by a sensor to achieve 90% of the total sensor response variation after the sensor is switched from a low RH value to high RH one) and the recovery times (the time necessary to reach 90% of the total resistance changes after the sensor is swapped from a high RH value to low RH one) at different humidity level, are summarized in Table 2 and Figure 9. First of all, only sensors BCu10_10L and BCU10_5L were able to detect 12% RH, while sensor BCu10_2L, though thinner than the previous ones, was sensitive from 20% RH and above, further confirming the prospect of doping DCPD with copper. Keeping the number of deposited layers constant, the sensor response increased with the copper content, whatever the relative humidity value (Table 2 and Figure 9).

Comparing the response times when switching the atmosphere from dry air to 50% or 90% relative humidity for different thicknesses, sensor BCu10 showed the fastest responses, while when reaching 28% RH, all the sensors had similar performances, whatever the copper content and the number of layers. Fast response times are due to the availability of adsorption sites [35]. Thus, copper addition is highly effective in favoring water molecule adsorption, and the higher the copper content, the lower the response time. Recovery times were generally longer than response times and increased with the number of layers and the copper content. Longer recovery times can be due to the capillary condensation of water vapor: when a higher number of layers are present, the water vapor is present in deeper layers of the surface, and water molecules need more time to desorb. Thicker films (made with 10 layers) also probably impose more difficult paths to water molecules when desorbing and could also contribute to long recovery times. The response and recovery times of these sensors can be considered reasonably fast for some applications.

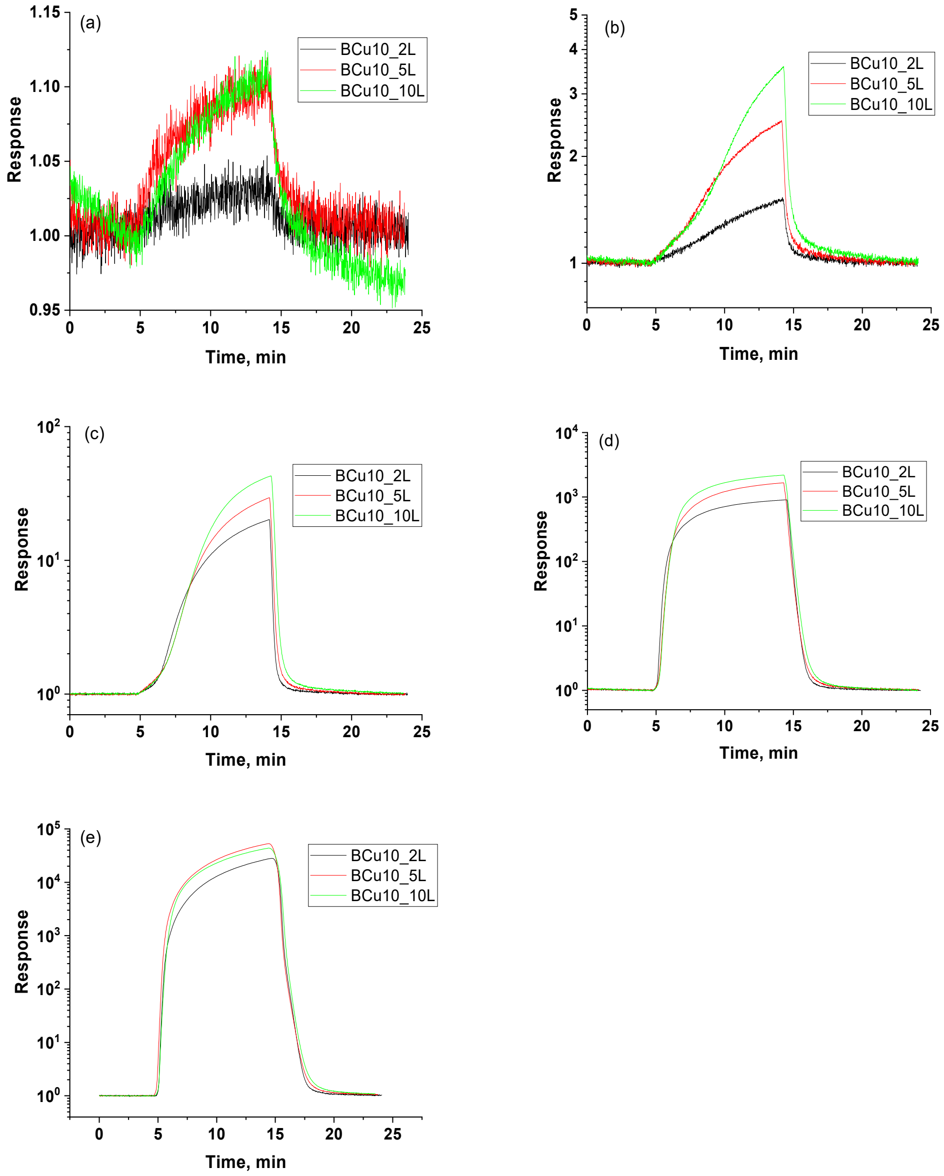

Figure 8. Sensor response in function of RH value for BCu10_10L, BCu10_5L, and BCu10_2L: (**a**) under 12% RH, (**b**) under 20% RH, (**c**) under 28% RH, (**d**) under 50% RH, and (**e**) under 90% RH.

Table 2. The sensor's response and response/recovery times at different humidity levels of the samples.

Sample	**Sensor Performance**	**Relative Humidity (%)**				
		90%	**50%**	**28%**	**20%**	**12%**
BCu10_10L	Sensor Response	43,750	2264	43	36	1.1
	Response/Recovery Time (s)	32/313	43/284	-	-	-
BCu10_5L	Sensor Response	51,250	1664	29	2.5	1.1
	Response/Recovery Time (s)	29/283	40/228	-	-	-

Table 2. *Cont.*

Sample	Sensor Performance	Relative Humidity (%)				
		90%	50%	28%	20%	12%
BCu10_2L	Sensor Response	26,892	907	20	1.6	-
	Response/Recovery Time (s)	24/257	35/170	-	-	-
BCu5_10L	Sensor Response	5963	31	1.4	-	-
	Response/Recovery Time (s)	38/238	153/153	-	-	-
BCu5_5L	Sensor Response	6265	20	1.4	-	-
	Response/Recovery Time (s)	38/229	150/176	-	-	-
BCu5_2L	Sensor Response	4315	13	1.2	-	-
	Response/Recovery Time (s)	43/155	205/78	220/147	-	-
BCu4_10L	Sensor Response	1907	6.3	1.3	-	-
	Response/Recovery Time (s)	66/211	-	223/277	-	-
BCu10_10L 1 year aged	Sensor Response	15,000	-	-	-	-
	Response/Recovery Time (s)	53/237	-	-	-	-

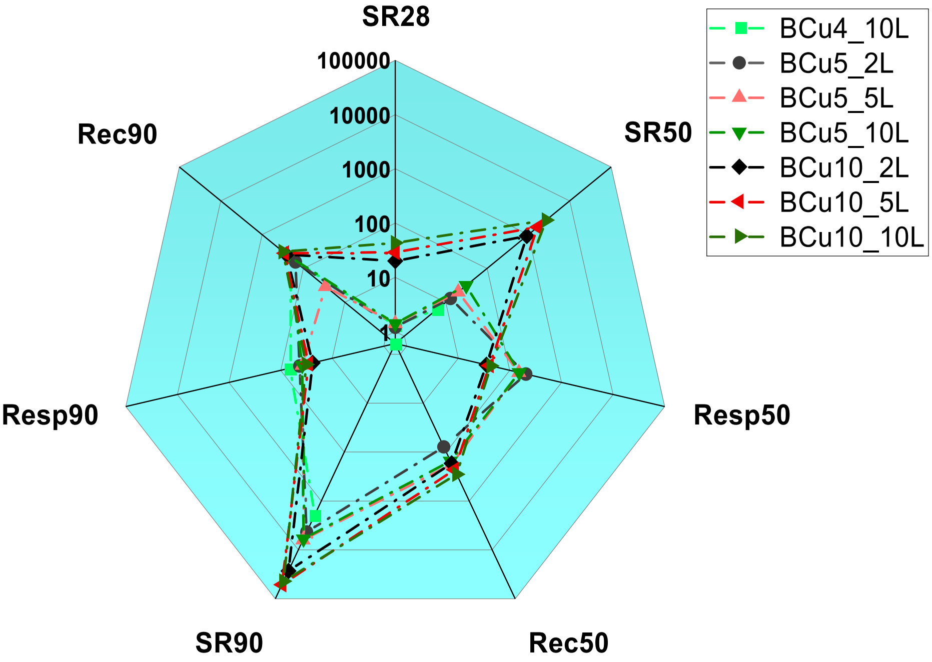

Figure 9. Radar plot of sensors features (SR28 = sensor response dry air—28% RH, SR50 = sensor response dry air—50% RH, Resp50 = response time dry air—50% RH, Rec50 = recovery time dry air—50% RH, SR90 = sensor response dry air—90% RH, Resp90 = response time dry air—90% RH, Rec90 = recovery time dry air—90% RH; for SR28, SR50 and SR90: the higher the values, the better, for resp50, resp90, rec50 and rec90: the lower the values, the better. Logarithmic scale).

Repeatability is also an essential characteristic for evaluating the humidity sensors' performances. Figure 10 displays three consecutive measurements on the BCu5_10L sensor after three pulses under 90% RH, starting from dry air. The sensor exhibited good repeatability and showed almost the same sensor response, response and recovery times as the previous tests.

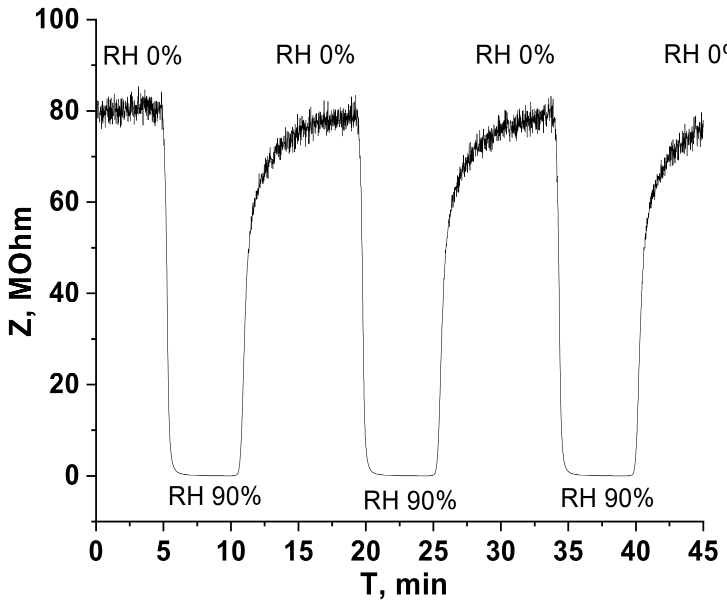

Figure 10. Repeatability measurements of the BCu5_10L sensor under 90% RH.

The calibration curves of the sensors are presented in Figure 11. The slopes (sensor sensitivity) are BCu4—0.052 RH^{-1}, BCu5—0.06 RH^{-1}, BCu10—0.06 RH^{-1}; BCu5_10L—0.06 RH^{-1}, BCu5_5L—0.059 RH^{-1}, BCu5_2L—0.058 RH^{-1}, BCu10_10L—0.06 RH^{-1}, BCu10_5L- 0.061 RH^{-1}, BCu10_2L—0.057 RH^{-1}, respectively, when log(R) is expressed in function of the relative humidity value.

The maximum hysteresis value of 8% was observed for the BCu10_10L sample under 90% RH (Figure 12).

The long-term stability of BCu10_10L sensors was evaluated after 1 year. Though brushite and monetite did not transform within 2 h of immersion into water [35], the response of the aged sensor was equal to 34% of that of the fresh one, and the response time increased by 60% compared to the response time of the fresh sample when switching from dry air to 90% RH (Figure 13).

The crystal structure of DCPD is made of compact sheets of parallel chains where calcium ions are coordinated by six oxygen atoms of phosphate groups and two oxygen atoms of the water molecules [36]. Two types of water molecules are present in DCPD: adsorbed and lattice water that can be electrolyzed with the subsequent proton migration. The modelling of neutron scattering analyses showed that local proton motions associated with jumps over two adjacent sites along the hydrogen bonds of the structure are possible [37]. DCP is made of $CaHPO_4$ chains bonded by Ca-O bonds and three types of hydrogen bonds. In addition, the unit cell contains two pairs of PO_4 units [37].

Hydroxyapatite (HAp, $Ca_{10}(PO_4)_6(OH)_2$, another calcium orthophosphate, was also investigated as a humidity-sensing material, and the adsorption of water molecules on it can be explained by the presence of hydroxyls at the center of Ca^{2+} triangles along the c-axis of the hexagonal cell [36]. In addition, several other ions are favorable sites for water molecule adsorption like the Ca^{2+}, $PO_4{}^{3-}$ and P-OH groups [36]. The charge carrier protons are transported along hydroxyls chains and via the jumping of protons from hydroxyls to near $PO_4{}^{3-}$. The high charge carrier density and electrostatic field favor proton mobility [36]. The same reactions were hypothesized in this work with DCP and sampleite, both being calcium phosphates.

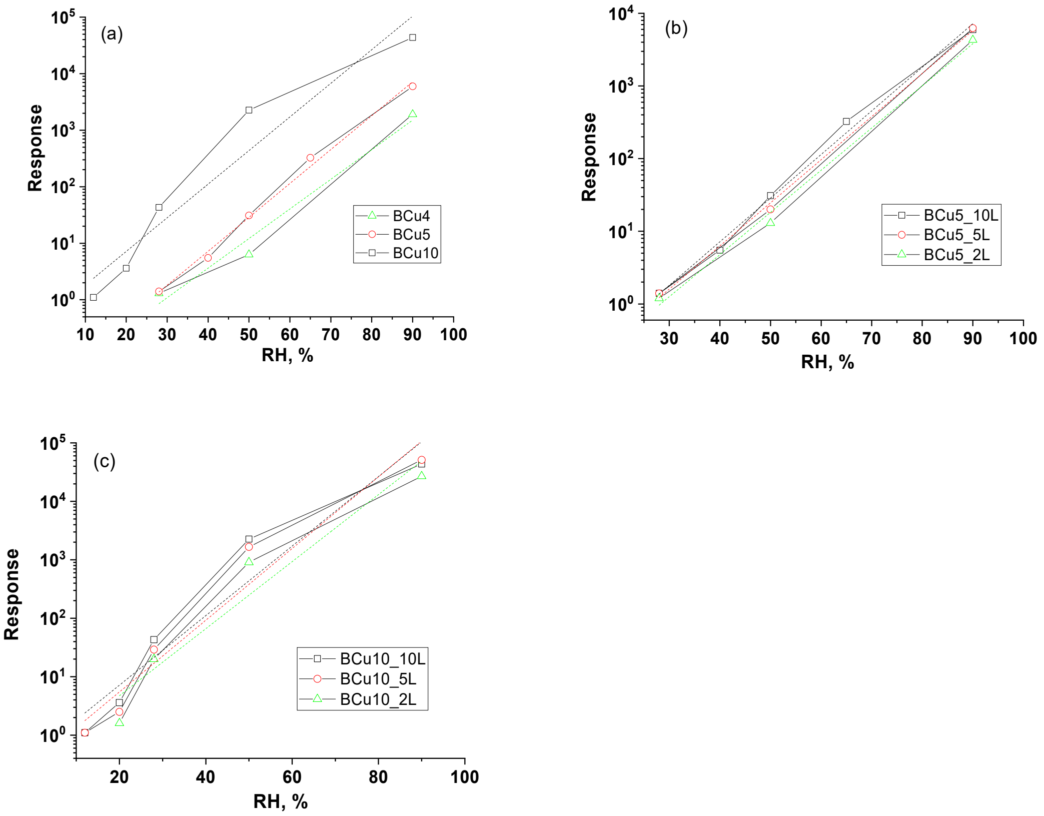

Figure 11. Calibration curves in the range of 10–90% RH for (**a**) BCu4, BCu5, BCu6, BCu10; (**b**) BCu5_10L, BCu5_5L, BCu5_2L; (**c**) BCu10_10L, BCu10_5L, BCu10_2L. The dashed lines represent the linear fit of the curves.

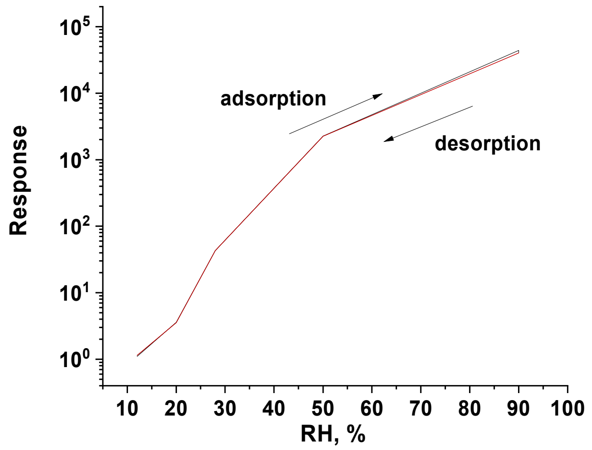

Figure 12. Sensor response in function of relative humidity value for BCu10_10L.

Moreover, the presence of copper atoms increases the number of adsorption sites and improves the sensors' response. Though CuO and Cu_2O were not detected by XRD, tenorite and cuprite are known humidity-sensing materials [38]. In addition, CuO-based heterostructures (CuO/ZnO and La_2CuO_4/ZnO) were studied as humidity sensors, and according to ref. [10], the sensing mechanism can be explained because of water electrolysis at the interface.

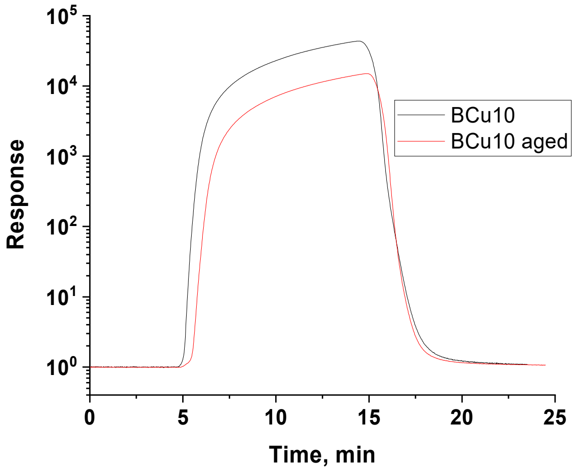

Figure 13. Impedance variation in function of relative humidity value under 90% RH for fresh prepared BCu10_10L (black) and 1-year aged BCu10_10L (red).

Gu et al. [39] investigated a CuO nanosheet-based humidity sensor. At the first stage of adsorption, under a low RH value, water molecules are mostly chemisorbed onto the available active sites of the sensor surface through a dissociative mechanism to form hydroxyl ions (OH^-) and proton (H^+) for two water molecules. The dissociation provides protons (H^+) as charge carriers hopping from site to site across the surface, leading to high impedance values. With the RH increase, more mobile protons are available from the water, and the impedance value decreases [39].

With further relative humidity increases, more water molecules are hydrogen-bonded to the hydroxyl groups and ionized to H_3O^+, increasing ion conductance and reducing impedance value [39].

When the RH is high, several continuous water layers are adsorbed on the sensor surface by physisorption. The surface-adsorbed water molecules undergo the following reactions:

$$2H_2O \leftrightarrow H_3O^+ + OH^- \tag{4}$$

$$H_2O + H_3O^+ \leftrightarrow H_3O^+ + H_2O \tag{5}$$

When the Grotthuss chain reaction mechanism is effective, the hydration of H_3O^+ is energetically favored in liquid water, and the protons move freely in the continuing liquid water layer [40].

Tests were also carried out at RT for nitrogenous oxide 2.5 ppm, methane 10 ppm, carbon dioxide 500 ppm and ammonia 4 ppm (Figures S2–S5, Supplementary information). The exposure time was 5 min and the test sequence did not impact sensor recovery. No interferences with the tested gases were noticed, so brushite-based sensors exhibited good selectivity with respect to humidity at RT.

Finally, Table 3 illustrates the results of the recent (in the last five years) literature data on resistive ceramic oxide humidity sensors. The studied sensors show interesting performances.

Table 3. Comparison of calcium orthophosphate-based humidity sensors' performances with recent literature data on resistive ceramic oxide sensors.

Material	**Sensor Response, R = Z_o/Z_g**	**Response Time, s**	**Recovery Time, s**	**Reference**
HAp composite GNP/HAp composite	5320% at 99% RH 18,680% at 99% RH	172 76	368 112	[36]
ZnO/MoS_2	~301 at 85% RH	138	166	[41]

Table 3. *Cont.*

Material	**Sensor Response, R = Z_o/Z_g**	**Response Time, s**	**Recovery Time, s**	**Reference**
Porous aluminum-doped ZnO	733% at 90% RH	∼238	~202	[42]
TiO_2 nanotubes	58.5 at 90% RH	NA	NA	[43]
$SrTiO_3$ nanoparticles	1.12 at 85% RH	100	300	[44]
Dy_2O_3 nanorods	15 at 97% RH	2	5	[45]
α-Fe_2O_3 nanoparticles	48,569 at 95% RH	9	4	[46]
$Cs_3Bi_2Br_9$ perovskite	987 at 90% RH	5.56	6.24	[47]
$Mn_{0\cdot5}Zn_{0.5}Dy_xHo_yFe_{2-x}O_4$ (x = 0.005 to 0.03) nanoparticles	99% at 97% RH	90	18	[48]
NHAp (natural hydroxyapatite)	17,900% at 87% RH	8	11	[49]
Al–Sr and Al–Cd nano-materials	2.87 at 95% RH 3.19 at 95% RH	60 44	29 45	[50]
Reduced graphene oxide/zinc oxide nanostructured powder	172 at 90% RH	NA	NA	[51]
$Zn_{x-1}Al_2O_4(TiO_2)_x$	265 at 97% RH	195	28	[52]
Ta-doped TiO_2/reduced graphene oxide	232% at 90% RH	4.2	3.3	[53]
N-doped graphene oxide-WO_3	3427 at 98% RH	24	53	[54]
Sr-doped $LaFeO_3$ nanofibers	60,597 at 90% RH	NA	NA	[55]
Mullite	322.9 at 85% RH	91	167	[56]
Ag/ZnO	151.8% under (11–95)% RH	36	6	[57]
CuO	3278% at 97.3% RH	49	12	[39]
ZnO-doped CuO	6045% under (30–90)% RH	6	7	[58]
Ce-doped ZnO thin film	10^8–10^4 Ω under (11–95)% RH	13	17	[59]
Mg-doped ZnO microspheres	under (11–95)% RH	24	12	[60]
Co-doped mesoporous TiO_2	1.39×10^5 at 90% RH	24	24	[61]
TiO_2-graphene	151% under (12–90)% RH	128	68	[62]
Ag-doped SnO_2 nanoparticles	under (11–98)% RH	4	6.5	[63]
SnO_2 nanowires	under (11–97)% RH	10	3	[64]
$(Ca_{1-x}Cu_x)HPO_4.nH_2O$ x = 0 to 1	51,250 at 90% RH	29	283	This work

4. Conclusions

Brushite-based materials with the gradual replacement of Ca^{2+} with Cu^{2+} ions were prepared by the chemical precipitation method. The synthesized powder was deposited onto interdigitated Pt electrodes using the spin coating method. Then, the sensors were tested from 0% to 90% relative humidity at RT.

Upon exposure to water vapor at 90% RH, the sensor response values were observed to be 43,750 for BCu10_10L, 5963 for BCu5_10L and 1907 for BCu4_10L. When assessing the sensitivity of samples BCu10 and BCu5 with different sensor layer thicknesses to RH, the BCu10_5L sample demonstrated a good response to RH at RT, starting from 12% RH. In contrast, the BCu5_5L sample showed lower sensitivity. A comparison of sensor performance at 90% humidity for BCu10 samples with different layer thicknesses showed that the best response and recovery times were achieved with a five-layer deposition, 29 and 283 s, respectively, and the highest response (51,250) was shown for BCu10_5L. The higher sensor's response and fast response and recovery times could be attributed to the introduction of Cu instead of Ca. Sensors exhibited good repeatability, and after 1 year of aging, the sensor response was equal to 34% of that of the fresh sensor response. The maximum value of hysteresis for BCu10_10L under 90% of RH was found to be 8%.

In addition, cross-sensitivity tests carried out on nitrogenous oxide 2.5 ppm, methane 10 ppm, carbon dioxide 500 ppm, and ammonia 4 ppm showed no interference. Thus, calcium orthophosphates are an interesting family of sensing materials. Future work should be devoted to understanding the aging phenomena of the sensing material.

Supplementary Materials: The following supporting information can be downloaded at: https://www.mdpi.com/article/10.3390/cryst15020153/s1, Figure S1: Sensor response under 90% RH for BCu0_10L and PVA_10L; Figure S2: Sensor response under 10 ppm CH_4 for BCu5_10L; Figure S3: Sensor response under 500 ppm CO_2 for BCu5_10L; Figure S4: Sensor response under 4 ppm NH_3 for BCu5_10L; Figure S5: Sensor response under 2.5 ppm NO_2 for BCu5_10L.

Author Contributions: Conceptualization, A.S.A. and J.-M.T.; methodology, all authors; investigation, Y.M., M.D. and A.S.A.; resources, A.S.A. and J.-M.T.; data curation, all authors; writing—original draft preparation, all authors; writing—review and editing, all authors; supervision, J.-M.T. All authors have read and agreed to the published version of the manuscript.

Funding: This research received no external funding.

Data Availability Statement: Data will be available on demand.

Acknowledgments: The authors are grateful to Mazen Alshaaer, Prince Sattam Bin Abdulaziz University, Saudi Arabia, for his support with the material synthesis.

Conflicts of Interest: The authors declare no conflicts of interest.

Abbreviations

The following abbreviations are used in this manuscript:

DCPD	Dicalcium phosphate dihydrate
DCP	Dicalcium phosphate
HAp	Hydroxyapathite
XRD	X-ray diffraction
FESEM	Field emission scanning electron microscopy

References

1. Sajid, M.; Khattak, Z.J.; Rahman, K.; Hassan, G.; Choi, K.H. Progress and future of relative humidity sensors: A review from materials perspective. *Bull. Mater. Sci.* **2022**, *45*, 238. [CrossRef]
2. Korotcenkov, G. *Handbook of Gas Sensor Materials, Properties, Advantages and Shortcomings for Applications, Vol. 2: New Trends and Technologies*; Springer: Berlin/Heidelberg, Germany, 2014. [CrossRef]
3. Tulliani, J.-M.; Inserra, B.; Ziegler, D. Carbon-Based Materials for Humidity Sensing: A Short Review. *Micromachines* **2019**, *10*, 232. [CrossRef] [PubMed]
4. Céline Laville, C.P.; Deletage, J.-Y. Humidity sensors for a pulmonary function diagnostic microsystem. *Sens. Actuators B Chem.* **2001**, *76*, 304–309. [CrossRef]
5. Tulliani, J.-M.; Baroni, C.; Zavattaro, L.; Grignani, C. Strontium-Doped Hematite as a Possible Humidity Sensing Material for Soil Water Content Determination. *Sensors* **2013**, *13*, 12070–12092. [CrossRef] [PubMed]
6. Traversa, E. Ceramic sensors for humidity detection: The state-of-the-art and future developments. *Sens. Actuators B* **1995**, *23*, 135–156. [CrossRef]
7. Arman Kuzubasoglu, B. Recent Studies on the Humidity Sensor: A Mini Review. *ACS Appl. Electron. Mater.* **2022**, *4*, 4797–4807. [CrossRef]
8. Ascorbe, J.; Corres, J.; Arregui, F.J.; Matias, I.R.; Mukhopadhyay, S.C. High Sensitivity Optical Structures for Relative Humidity Sensing. In *Smart Sensors, Measurement and Instrumentation, Vol. 23, Sensors for Everyday Life*; Environmental and Food Engineering;

Mukhopadhyay, S.C., Postolache, O.A., Jayasundera, K.P., Swain, A.K., Eds.; Springer: Berlin/Heidelberg, Germany, 2017; pp. 55–80. [CrossRef]

9. Fraden, J. *Handbook of Modern Sensors. Physics, Designs and Applications*, 5th ed.; Springer: Berlin/Heidelberg, Germany, 2016; pp. 507–524. [CrossRef]
10. Korotcenkov, G. *Handbook of Gas Sensor Materials, Properties, Advantages and Shortcomings for Applications, Vol. 1: Conventional Approaches*; Springer: Berlin/Heidelberg, Germany, 2013; pp. 389–408. [CrossRef]
11. Farahani, H.; Wagiran, R.; Hamidon, M.N. Humidity Sensors Principle, Mechanism, and Fabrication Technologies: A Comprehensive Review. *Sensors* **2014**, *14*, 7881–7939. [CrossRef]
12. Sun, L.; Haidry, A.H.; Fatima, Q.; Li, Z.; Yao, Z. Improving the humidity sensing below 30% RH of TiO2 with GO modification. *Mater. Res. Bull.* **2018**, *99*, 124–131. [CrossRef]
13. Staerz, A.; Berthold, C.; Russ, T.; Wicker, S.; Weimar, U.; Barsan, N. The oxidizing effect of humidity on WO3 based sensors. *Sens. Actuators B Chem.* **2016**, *237*, 54–58. [CrossRef]
14. Esteban-Cubillo, A.; Tulliani, J.-M.; Pecharromán, C.; Moya, J.S. Iron-oxide nanoparticles supported on sepiolite as a novel humidity sensor. *J. Eur. Ceram. Soc.* **2007**, *27*, 1983–1989. [CrossRef]
15. Ataalla, M.; Afify, A.S.; Hassan, M.; Adam, A.M.; Milanova, M.; Piroeva, I. Humidity Sensing Properties of Tungsten Based Glass Crystalline Materials in the WO3-ZnO-La2O3-Al2O3 System. In *NATO Science for Peace and Security Series B: Physics and Biophysics*; Springer: Dordrecht, The Netherlands, 2018; pp. 417–425. [CrossRef]
16. Wang, W.; Virkar, A.V. A conductimetric humidity sensor based on proton conducting perovskite oxides. *Sens. Actuators B* **2004**, *98*, 282–290. [CrossRef]
17. Zhao, J.; Liu, Y.; Li, X.; Lu, G.; You, L.; Liang, X.; Liu, F.; Zhang, T.; Du, B. Highly sensitive humidity sensor based on high surface area mesoporous $LaFeO_3$ prepared by a nanocasting route. *Sens. Actuators B Chem.* **2013**, *181*, 802–809. [CrossRef]
18. Wang, J.; Wu, F.Q.; Shi, K.H.; Wang, X.H.; Sun, P.P. Humidity sensitivity of composite material of lanthanum ferrite/polymer quaternary acrylic resin. *Sens. Actuators B Chem.* **2004**, *99*, 586–591. [CrossRef]
19. Cho, M.Y.; Kim, S.; Kim, I.S.; Kim, E.S.; Wang, Z.J.; Kim, N.Y.; Kim, S.W.; Oh, J.M. Perovskite-Induced Ultrasensitive and Highly Stable Humidity Sensor Systems Prepared by Aerosol Deposition at Room Temperature. *Adv. Funct. Mater.* **2019**, *30*, 1907449. [CrossRef]
20. Hikku, G.S.; Arthi, C.; Robert, R.J.; Jeyasubramanian, K. Calcium phosphate conversion technique: A versatile route to develop corrosion resistant hydroxyapatite coating over Mg/Mg alloys based implants. *J. Magnes. Alloys* **2022**, *10*, 1821–1845. [CrossRef]
21. Kong, Y.; Ma, R.; Li, G.; Wang, G.; Liu, Y.; Yuan, J. Impact of biochar, calcium magnesium phosphate fertilizer and spent mushroom substrate on humification and heavy metal passivation during composting. *Sci. Total Environ.* **2022**, *824*, 153755. [CrossRef] [PubMed]
22. Paknahad, A.; Kucko, N.W.; Leeuwenburgh, S.C.G.; Sluys, L.J. Experimental and numerical analysis on bending and tensile failure behavior of calcium phosphate cements. *J. Mech. Behav. Biomed. Mater.* **2020**, *107*, 1033565. [CrossRef] [PubMed]
23. Sánchez-Paniagua López, M.; Tamimi, F.; López-Cabarcos, E.; López-Ruiz, B. Highly sensitive amperometric biosensor based on a biocompatible calcium phosphate cement. *Biosens. Bioelectron.* **2009**, *24*, 2574–2579. [CrossRef] [PubMed]
24. Sudhan, N.; Anitta, S.; Meenakshi, S.; Sekar, C. Brushite nanoparticles based electrochemical sensor for detection of uric acid, xanthine, hypoxanthine and caffeine. *Anal. Biochem.* **2022**, *659*, 114947. [CrossRef]
25. Sánchez-Paniagua López, M.; Redondo-Gómez, E.; López-Ruiz, B. Electrochemical enzyme biosensors based on calcium phosphate materials for tyramine detection in food samples. *Talanta* **2017**, *175*, 209–216. [CrossRef] [PubMed]
26. Alshaaer, M.; Al-Kafawein, J.; Afify, A.S.; Hamad, N.; Saffarini, G.; Issa, K. Effect of Ca2+ Replacement with Cu2+ Ions in Brushite on the Phase Composition and Crystal Structure. *Minerals* **2021**, *11*, 1028. [CrossRef]
27. Bohner, M.; Merkle, H.P.; Lemaître, J. In vitro aging of a calcium phosphate cement. *J. Mater. Sci. Mater. Med.* **2000**, *11*, 155–162. [CrossRef] [PubMed]
28. Di Francia, E.; Guzmán, H.; Pugliese, D.; Hernández, S.; Tulliani, J.M. Nanostructured Cu/Zn/Al-based oxide as a new sensing material for NO_2 detection. *Sens. Actuators B Chem.* **2024**, *420*, 136456. [CrossRef]
29. Available online: https://gml.noaa.gov/ccgg/trends (accessed on 20 January 2025).
30. Available online: https://www.unep.org/resources/report/air-quality-guidelines-europe-second-edition (accessed on 20 January 2025).
31. Available online: https://gml.noaa.gov/ccgg/trends_ch4 (accessed on 20 January 2025).
32. Petrus, M.; Popa, C.; Bratu, A.M. Ammonia Concentration in Ambient Air in a Peri-Urban Area Using a Laser Photoacoustic Spectroscopy Detector. *Materials* **2022**, *15*, 3182. [CrossRef] [PubMed]
33. Available online: https://winter.group.shef.ac.uk/webelements/index.html (accessed on 20 January 2025).
34. Alshaaer, M. Microstructural characteristics and long-term stability of wollastonite-based chemically bonded phosphate ceramics. *Int. J. Appl. Ceram. Technol.* **2021**, *18*, 319–331. [CrossRef]

35. Lu, B.-Q.; Willhammar, T.; Sun, B.-B.; Hedin, N.; Gale, J.D.; Gebauer, D. Introducing the crystalline phase of dicalcium phosphate monohydrate. *Nat. Com.* **2020**, *11*, 1546. [CrossRef] [PubMed]
36. Kumar, S.; Yadav, N.; Singh, P. Effect of graphene weight percentage on surface morphology and humidity-sensing performances of hydroxyapatite/graphene nanocomposite. *J. Mater. Sci. Mater. Electron.* **2024**, *35*, 2238. [CrossRef]
37. Tortet, L.; Gavarri, J.R.; Nihoul, G.; Dianoux, A.J. Proton mobilities in brushite and brushite/polymer composites. *Solid. State Ion.* **1997**, *97*, 253–256. [CrossRef]
38. Nunes, D.; Pimentel, A.; Gonçalves, A.; Pereira, S.; Branquinho, R.; Barquinha, P.; Fortunato, E.; Marti, R. Metal oxide nanostructures for sensor applications. *Semicond. Sci. Technol.* **2019**, *34*, 043001. [CrossRef]
39. Gu, Y.; Jiang, H.; Ye, Z.; Sun, N.; Kuang, X.; Liu, W.; Li, G.; Song, X.; Zhang, L.; Bai, W.; et al. Impact of Size on Humidity Sensing Property of Copper Oxide Nanoparticles. *Electron. Mater. Lett.* **2020**, *16*, 61–71. [CrossRef]
40. Agmon, N. The Grotthuss mechanism. *Chem. Phys. Lett.* **1995**, *244*, 456–462. [CrossRef]
41. Burman, D.; Choudhary, D.S.; Guha, P.K. ZnO/MoS2-based enhanced humidity sensor prototype with android app interface for mobile platform. *IEEE Sens. J.* **2019**, *19*, 3993–3999. [CrossRef]
42. Kundu, S.; Majumder, R.; Ghosh, R.; Pal Chowdhury, M. Superior positive relative humidity sensing properties of porous nanostructured Al:ZnO thin films deposited by jet-atomizer spray pyrolysis technique. *J. Mater. Sci. Mater. Electron.* **2019**, *30*, 4618–4625. [CrossRef]
43. Manut, A.; Zoolfakar, A.S.; Mamat, M.H.; Ab Ghani, N.S.; Zolkapli, M. Characterization of Titanium Dioxide (TiO_2) Nanotubes for Resistive-type Humidity Sensor. In Proceedings of the IEEE International Conference on Semiconductor Electronics (ICSE), Kuala Lumpur, Malaysia, 28–29 July 2020; pp. 104–107.
44. Duy, L.T.; Baek, J.Y.; Mun, Y.J.; Seo, H. Patternable production of SrTiO3 nanoparticles using 1-W laser directly on flexible humidity sensor platform based on ITO/SrTiO3/CNT. *J. Mater. Sci. Technol.* **2021**, *71*, 186–194. [CrossRef]
45. Yasin, E.; Javed, Y.; Imran, Z.; Anwar, H.; Shahid, M. Exploration of dielectric and humidity sensing properties of dysprosium oxide nanorods. *Eur. Phys. J. Plus* **2023**, *138*, 1050. [CrossRef]
46. Dhariwal, N.; Yadav, P.; Kumari, M.; Jain, P.; Sanger, A.; Kumar, V.; Thakur, O.P. Iron oxide-based nanoparticles for fast-response humidity sensing, real-time respiration monitoring, and noncontact sensing. *IEEE Sens. J.* **2023**, *23*, 22217–22224. [CrossRef]
47. Pi, C.; Chen, W.; Zhou, W.; Yan, S.; Liu, Z.; Wang, C.; Guo, Q.; Qiu, J.; Yu, X.; Liu, B.; et al. Highly stable humidity sensor based on lead-free Cs3Bi2Br9 perovskite for breath monitoring. *J. Mater. Chem. C* **2021**, *9*, 11299–11305. [CrossRef]
48. El-Denglawey, A.; Manjunatha, K.; Vijay Sekhar, E.; Chethan, B.; Zhuang, J.; Jagadeesha Angadi, V. Rapid response in recovery time, humidity sensing behavior and magnetic properties of rare earth(Dy & Ho) doped Mn–Zn ceramics. *Ceram. Int.* **2021**, *47*, 28614–28622. [CrossRef]
49. Khtaoui, L.; Laghrouche, M.; Fernane, F.; Chaouchi, A. High-sensitivity humidity sensor based on natural hydroxyapatite. *J. Mater. Sci. Mater. Electron.* **2021**, *32*, 8668–8686. [CrossRef]
50. Shah, Z.; Shaheen, K.; Arshad, T.; Ahmad, B.; Khan, S.B. Al doped Sr and Cd metal oxide nanomaterials for resistive response of humidity sensing. *Mater. Chem. Phys.* **2022**, *290*, 126632. [CrossRef]
51. Subki, A.S.R.A.; Mamat, M.H.; Musa, M.Z.; Abdullah, M.H.; Shameem Banu, I.B.; Vasimalai, N.; Ahmad, M.K.; Nafarizal, N.; Suriani, A.B.; Mohamad, A.; et al. Effects of varying the amount of reduced graphene oxide loading on the humidity sensing performance of zinc oxide/reduced graphene oxide nanocomposites on cellulose filter paper. *J. Alloys Compd.* **2022**, *926*, 166728. [CrossRef]
52. Dubey, R.S.; Srilali, S.; Ravikiran, Y.T.; Babu, G.S.; Katta, K.V. Synthesis and characterization of Znx-1Al2O4(TiO2)x nanocomposite ceramics and their humidity sensing properties. *J. Mater. Sci.* **2022**, *57*, 2636–2649. [CrossRef]
53. Mohamed Zahidi, M.; Mamat, M.H.; Subki, A.S.R.A.; Abdullah, M.H.; Hassan, H.; Ahmad, M.K.; Bakar, S.A.; Mohamed, A.; Ohtani, B. Formation of a nanorod-assembled TiO_2 actinomorphic-flower-like microsphere film via Ta doping using a facile solution immersion method for humidity sensing. *Nanomaterials* **2023**, *13*, 256. [CrossRef]
54. Ravichandran, R.; Quine, S.D.; Arularasu, M.V. Humidity sensing performance of nitrogen doped reduced graphene oxide-WO3 composite. *Bio Nano Sci.* **2023**, *13*, 2205–2214. [CrossRef]
55. Zhang, Z.; Li, F.; Zheng, Y. Highly sensitive resistive humidity sensor based on strontium-doped lanthanum ferrite nanofibers. *Sens. Actuators A Phys.* **2023**, *358*, 114435. [CrossRef]
56. Milovanov, Y.; Bertero, A.; Coppola, B.; Palmero, P.; Tulliani, J.-M. Mullite 3D Printed Humidity Sensors. *Ceramics* **2024**, *7*, 807–820. [CrossRef]
57. Li, P.; Yu, S.; Zhang, H. Preparation and Performance Analysis of Ag/ZnO Humidity Sensor. *Sensors* **2021**, *21*, 857. [CrossRef] [PubMed]
58. Zainelabdin, A.; Amin, G.; Zaman, S.; Nur, O.; Lu, J.; Hultman, L.; Willander, M. CuO/ZnO nanocorals synthesis via hydrothermal technique: Growth mechanism and their application as humidity sensor. *Mater. Chem.* **2012**, *22*, 11583–11590. [CrossRef]
59. Anbia, M.; Fard, S.E.M. Humidity sensing properties of Ce-doped nanoporous ZnO thin film prepared by sol-gel method. *J. Rare Earths* **2012**, *30*, 38–42. [CrossRef]

60. Lin, C.; Zhang, H.; Zhang, J.; Chen, C. Enhancement of the humidity sensing performance in Mg-doped hexagonal ZnO microspheres at room temperature. *Sensors* **2019**, *19*, 519. [CrossRef]
61. Li, Z.; Haidry, A.A.; Gao, B.; Wang, T.; Yao, Z. The effect of Co-doping on the humidity sensing properties of ordered mesoporous TiO_2. *Appl. Surf. Sci.* **2017**, *412*, 638–647. [CrossRef]
62. Lin, W.D.; Liao, C.T.; Chang, T.C.; Chen, S.H.; Wu, R.J. Humidity sensing properties of novel graphene/TiO_2 composites by sol–gel process. *Sens. Actuators B Chem.* **2015**, *209*, 555–561. [CrossRef]
63. Tomer, V.K.; Duhan, S. A facile nanocasting synthesis of mesoporous Ag-doped SnO_2 nanostructures with enhanced humidity sensing performance. *Sens. Actuators B Chem.* **2016**, *223*, 750–760. [CrossRef]
64. Gao, N.; Li, H.Y.; Zhang, W.; Zhang, Y.; Zeng, Y.; Zhixiang, H.; Liu, J.; Jiang, J.; Miao, L.; Yi, F.; et al. QCM-based humidity sensor and sensing properties employing colloidal SnO_2 nanowires. *Sens. Actuators B Chem.* **2019**, *293*, 129–135. [CrossRef]